

pubs.acs.org/IECR Article

Kinetic Assessment of Light Hydrocarbons Separation over Fe-Doped 13X Composite Sorbents Under Multicomponent Feed **Conditions**

Khaled Baamran, Jimmy D. L. Moreno, Ali A. Rownaghi, and Fateme Rezaei*

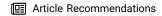


Cite This: Ind. Eng. Chem. Res. 2023, 62, 11917-11929



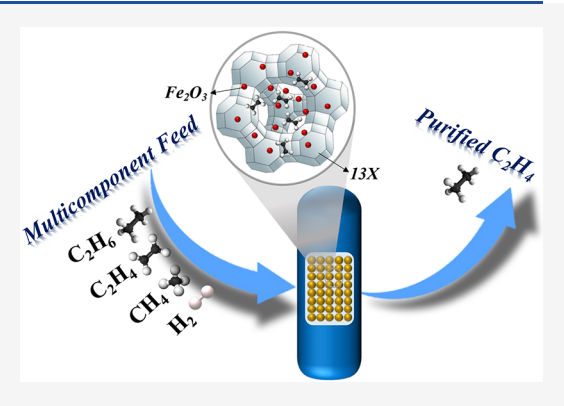
ACCESS

III Metrics & More



s Supporting Information

ABSTRACT: Current sorbents investigated for light olefin/paraffin separation usually suffer from low selectivity. Besides, multicomponent analysis of this important separation is usually overlooked in the literature. To enhance the separation efficiency of zeolite 13X, we developed a series of Fe₂O₃/13X composite sorbents and assessed their separation performance using binary, ternary, and multicomponent gas mixtures of C₂H₄, C₂H₆, CH₄, and H₂. In these composites, nano- and micro Fe₂O₃ particles (NPs and MPs) with varied loadings were used, while Fe was also ion-exchanged into the 13X zeolite structure. The microporosity and surface area of the bare sorbent were reduced upon increasing Fe, loading for all particle sizes. However, Fe₁(NPs)/ 13X demonstrated a higher C₂H₄ adsorption capacity and C₂H₄/C₂H₆ selectivity despite its lower surface area, which was attributed to its higher surface electron transfer property that enhanced its adsorption performance



via electrostatic interactions. Additionally, the incorporation of Fe₁ into the 13X framework resulted in narrowing of the micropore channels, thereby promoting the molecular sieving effect and improving the selectivity toward C₂H₄. The dynamic adsorption results revealed the reduction in $C_2H_4/(C_2H_6 + CH_4 + H_2)$ selectivity in the presence of impurity gases (CH₄ and H₂), from 4.10 to 3.84 and 3.20 for binary, ternary, and multicomponent gas mixtures, respectively. Nevertheless, the C₂H₄/C₂H₆ selectivity was found to be roughly constant at ~4 across all feed conditions. Moreover, the affinity of Fe₁(NPs)/13X toward different adsorbates from the most adsorbed to the least adsorbed component was in the order of $C_2H_4 > C_2H_6 > CH_4 > H_2$, while the rates of species transport were found to be primarily dependent on the rates of molecular diffusion within the pores of the 13X zeolite.

1. INTRODUCTION

Ethylene and propylene are the two major products of the petrochemical industry with an annual production of ~300 MT and a carbon footprint of >500 MT CO₂ equiv. ¹⁻³ These chemical building blocks are traditionally produced through steam cracking of naphtha and used extensively in polymers and plastics production. 4-6 Recently, oxidative coupling of CH₄ (OCM) has received considerable attention for converting CH₄ into ethylene (C₂H₄) using heterogeneous catalysts. The C₂H₄ produced from OCM is however typically mixed with unwanted byproducts such as C₂H₆, CH₄, and H₂. As a result, further purification is required to purify C₂H₄ for utilization as a feedstock. Adsorption-based separations offer a great potential to replace the traditional cryogenic distillation and fulfill the energy-efficient separation economy in olefin/ paraffin separations. The separation of C_2H_4/C_2H_6 is especially challenging because of the similarities in their physical properties such as boiling point, molecular weight, and kinetic diameter. 11-13

Zeolites, 14,15 alumina, 16 and carbon-based materials 17-19 are common sorbents for C2H4 purification. Metal-organic frameworks (MOFs), on the other hand, have recently been explored in C₂H₆/C₂H₄ separation.²⁰⁻²² Although MOFs appear to be excellent candidates for this important separation, their weak stability and high cost make them less desirable compared to the traditional sorbents.^{23–25} Like MOFs, 13X zeolite displays strong preferential adsorption of C2H4 over C₂H₆ and other byproducts; however, unlike open-metal-site MOFs, its high selectivity stems from π -ion interactions between π bonds of C_2H_4 and electropositive cations (Na⁺) and not because of the $\pi-\pi$ complexation interactions.^{7,26-28}

In this work, we hypothesized that the presence of iron oxides will contribute to the establishment of unsaturated surface bonds to strengthen dipole-quadrupole electrostatic interactions between the adsorbate molecules (C2H4) and the 13X sorbent, thereby facilitating their polarization and subsequent capture. Previous studies have explored the

February 26, 2023 Received: Revised: June 23, 2023 Accepted: June 30, 2023 Published: July 24, 2023





possibility of enhanced CO₂ capture over iron oxide/13X composites relative to the bare zeolite. For instance, Popova et al. 29 found that introducing iron oxides or Fe $^{2+/3+}$ ions into the NaX zeolite structure enhances CO2 adsorption, thanks to the specific state of iron within the zeolite. Similarly, Chanapattharapol et al.³⁰ investigated the use of iron oxide-doped silica (MCM-41) for CO₂ capture and observed improved CO₂ adsorption compared to the bare MCM-41. The optimal result was achieved with 0.50 wt % Fe/MCM-41. The enhanced adsorption can be attributed to electron transfer from dorbitals to π -antibonding orbitals of CO₂, leading to stronger attraction between the CO2 molecules and iron oxide-doped zeolite or silicate, thereby improving the overall adsorption performance. In a recent publication, Xiang et al.³¹ conducted a study on iron-containing 13X zeolite (Fe@13X) and its direct air capture (DAC) capability. Their research findings indicated that relative to the bare 13X, Fe@13X exhibited superior performance in terms of capture capacity and productivity. This improvement was attributed to the introduction of iron atoms into the zeolite structure, which increased the electronegativity of the sorbent and narrowed the micropore channels.

To test our hypothesis and to develop efficient sorbents for olefin/paraffin separation, we aimed at developing Fe₂O₃doped 13X zeolite composites and assessing their separation efficiency in binary, ternary, and multicomponent feed streams. Although a variety of contaminants or impurity gases should be considered for the light olefin/paraffin separation, we confined ourselves to the most important multicomponent stream of C₂H₆, CH₄, and H₂. In this regard, three main sorbents comprising Fe₂O₃ nanoparticles (NPs), Fe₂O₃ microparticles (MPs), and Fe₂O₃ (ion exchanged) were developed through impregnation method and characterized accordingly. The preliminary adsorption results showed that Fe₂O₂(NPs)/13X outperformed its counterparts; thus, the Fe₂O₃ composition was varied to optimize its loading for this particular sorbent. The binary, ternary, and multicomponent breakthrough experiments were performed at different feed flow rates and the corresponding adsorption capacities, desorption rates, and selectivity values were estimated accordingly. Finally, the overall mass transfer coefficients and diffusivities were estimated by modeling the concentration profiles from binary, ternary, and multicomponent trials.

2. EXPERIMENTAL SECTION

- **2.1. Materials.** The following materials were used in sorbent synthesis without further purification: iron(III) oxide microparticles (Fe₂O₃, alpha, 99.5%, < 5 μ m), iron(III) oxide nanoparticles (Fe₂O₃, alpha, 99.5%, 30 nm), iron(III) nitrate nonahydrate Fe(NO₃)₃(H₂O)₉, and 13X zeolite. All materials were purchased from Sigma-Aldrich except for the zeolite, which was purchased from UOP Honeywell Company. The ultrahigh purity (UHP) gases used in this study were obtained from Airgas.
- **2.2. Synthesis of Fe**_x/13X **Sorbents.** For Fe₂O₃-doped sorbent synthesis, a wet impregnation method was used. Briefly, various amounts of Fe₂O₃ (Fe_x, where x = 1, 5, and 10 wt % for NPs, and 5 wt % for MPs and ion-exchanged sample) were dispersed in DI water, and the solution was then stirred vigorously at 500 rpm for 5 h. The obtained materials were dried overnight at 120 °C, and the precipitations were ground into homogeneous powder using a mortar and pestle. For synthesis of iron ion-exchanged 13X, the calcined 13X zeolite

was introduced to the Fe(NO₃)₃(H₂O)₉ solution, following a method reported in the literature with some modifications. First, 13X was calcined at 500 °C using a muffle furnace for 5 h before it was dispersed in 5 wt % Fe(NO₃)₃(H₂O)₉ solution for 12 h, followed by vacuum filtration with extensive DI water. The as-synthesized product was then dried at 120 °C overnight and calcined again at 500 °C for 5 h at a 10 °C/min heating rate. The prepared samples, namely, Fe₁(30 nm)/13X, Fe₅(30 nm)/13X, Fe₁₀(30 nm)/13X, Fe₅(5 μ m)/13X, and Fe₅(ion-exchange)/13X, were labeled as Fe₁(NPs)/13X, Fe₅(NPs)/13X, Fe₁₀(NPs)/13X, Fe₅(MPs)/13X, and Fe₅(Ion)/13X, respectively. It should be noted that the reported particle size values represent the average measurements for these materials.

- **2.3. Characterization of Fe_x/13X Sorbents.** The textural properties of the Fe_x/13X samples were assessed by N₂ physisorption experiments at 77 K using a Micromeritics (3Flex) gas analyzer instrument. All of the samples $(Fe_1(NPs)/$ 13X, $Fe_5(NPs)/13X$, $Fe_{10}(NPs)/13X$, $Fe_5(MPs)/13X$, and Fe₅(Ion)/13X) were degassed before analysis at 350 °C for 5 h under vacuum on a Micromeritics Smart VacPrep instrument. The Brunauer-Emmett-Teller (BET) and nonlocal density functional theory (NLDFT) methods were used to determine the BET surface area, and pore size distribution (PSD) and pore volume, respectively. The setting parameters of the BET and NLDFT methods are included in the Supporting Information. It should be noted here that the Rouquerol criteria in the 3Flex analyzer are typically determined by selecting a range of relative pressures (P/P_0) , where the adsorption data are most linear, i.e., the plot of $(1 - (P/P_0))$ versus P/P_0 is linear. The linear range was selected for the calculation of the BET surface area using the slope and intercept of the linear portion of the plot.
- 2.4. Unary Adsorption Isotherm Measurements. A volumetric gas analyzer (Micromeritics, 3Flex) was utilized to measure the adsorption isotherms of C_2H_6 , C_2H_4 , CH_4 , and H_2 over a pressure range of 0-1 bar. Prior to the measurements, 13X, $Fe_1(NPs)/13X$, $Fe_5(NPs)/13X$, $Fe_{10}(NPs)/13X$, Fe₅(MPs)/13X, and Fe₅(Ion)/13X were degassed on the Micromeritics Smart VacPrep instrument under vacuum at 350 °C for 5 h to remove any preadsorbed gas or moisture. The equilibrium adsorption isotherms were fitted using the Sips model to describe the adsorption process over the synthesized sorbents, as shown in eq S7, Supporting Information. The elemental composition and concentration of the sorbents were determined by using inductively coupled plasma mass spectrometry (ICP-MS). The focused ion beam/scanning electron microscopy-Helios Hydra CX system from Thermo Fisher Scientific (FIB-SEM) and energy-dispersive spectrometry (EDS) were also employed to assess the elemental dispersion of the sorbents and their surface topography. The oxidation states of Fe were determined using X-ray photoelectron spectroscopy (XPS) on a Thermo Scientific Nexsa 128 channel XPS system.
- **2.5. Dynamic Adsorption Experiments.** The dynamic adsorption—desorption experiments were carried out in a stainless-steel fixed bed column of 1 cm inner diameter and 12 cm length. The typical operating conditions used in all breakthrough experiments were 25 °C, 1 bar, and 2 g of sorbent mass. Before each test, all the samples were *in situ* activated at 200 °C for 8 h under 20 mL/min Ar flow. Next, the adsorption bed was cooled down to 25 °C and a gas feed with a composition of 1:1 volume ratio of C₂H₆ and C₂H₄ was

flowed into the column at 54 mL/min simultaneously with 13 mL/min of Ar. The temperature change across the bed's inlet and outlet was monitored by a thermocouple (Figure 1),

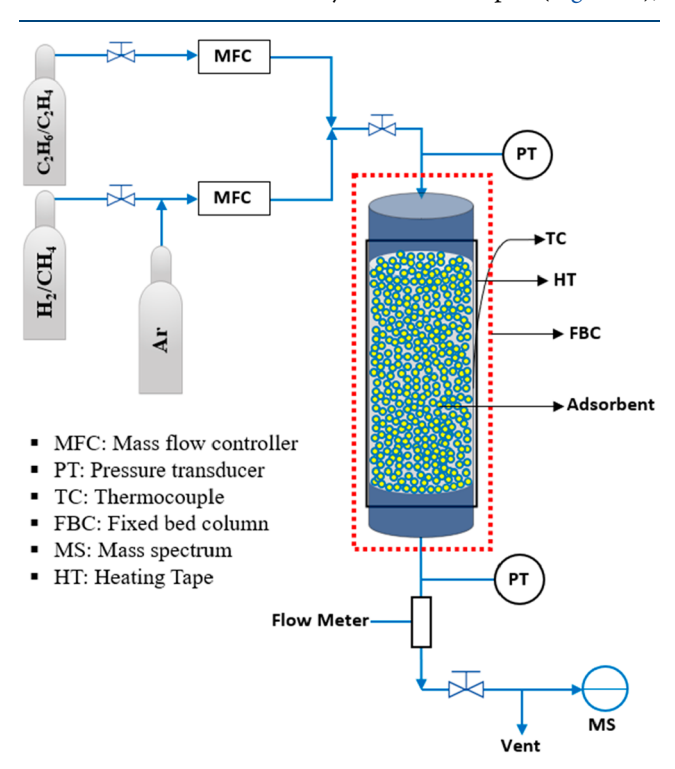


Figure 1. Schematic representation of the experimental setup used in the breakthrough experiments.

however, any potential internal temperature changes occurring during adsorption/desorption steps were disregarded in this study, as they were expected to be within a manageable (nearly isothermal) range based on our previous research. The gas flow rate was controlled by mass flow controllers (MFCs, Brooks) and the outlet gas flow was analyzed by a mass spectrometer (MKS, Cirrus 2), as shown in Figure 1. The steps were repeated until the bed was fully saturated with $\rm C_2H_6$ and $\rm C_2H_4$. Here, the term "full saturation" (or pseudo-equilibrium) refers to the point at which the concentrations of adsorbates in the outlet become very close to (or match) their initial

concentrations in the inlet $(C_i/C_0 = 1)$. After achieving full saturation, the gas flow was continued for several more minutes to ensure that pseudo-equilibrium had been reached. Subsequently, the flow of the feed gas was switched to 20 mL/min of Ar. Finally, the temperature was raised from 25 to 200 °C. The desorption step was continued until no C₂H₆ and C₂H₄ were observed at the column outlet. The adsorptiondesorption experiments were repeated with the same procedure for ternary and multicomponent runs. The blank run was also conducted with an empty column (i.e., the column was filled only with glass wool). The duration it took for the gas signal to appear in the mass spectrometer was referred to as the lag time and was subtracted from the retention time of the gas recorded during actual experiments.34,35 This correction was applied whenever there were changes in the operating conditions. It is worth noting here that at the threshold of mixing moment, it is possible for the feed components with the lower flow rate to experience a delay in retention time, followed by a sudden surge in the adsorption column. This surge is a result of the expected pressure gradient during premixing that arises from the combination of different flow rates at the beginning of adsorption. To have an accurate estimation of the amount of gas adsorbed, we subtracted the lag time from the retention time of the gas after adsorption in the column.

2.6. Kinetic Analysis of Multicomponent Separation. Bulk phase mass balance (eq S4) was used to investigate the gas adsorption kinetics. The model in eq S4 and eq S5 was used to estimate the mass transfer coefficient (\bar{k}, s^{-1}) via fitting the breakthrough curves. The molecular diffusivity $(D_{m,i}, cm^2/s)$, film mass transfer coefficient $(k_{fr}, cm/s)$, particle mass transfer coefficient $(k_{fr}, cm/s)$, axial dispersion $(D_L, cm^2/s)$, and effective diffusivity $(D_{effr}, cm^2/s)$ were calculated by eq S13–S21, respectively, while the overall mass transfer coefficient $(k_{overall}, s^{-1})$ was estimated by eq S22, Supporting Information. The models were solved using the approximate order derivative method in MATLAB (by the ODE15s function) after slicing the partial differential equations (PDEs) into several ordinary differential equations (ODEs).

3. RESULTS AND DISCUSSION

3.1. Characterization of $Fe_x/13X$ Sorbents. The morphologies and the corresponding EDS mapping images

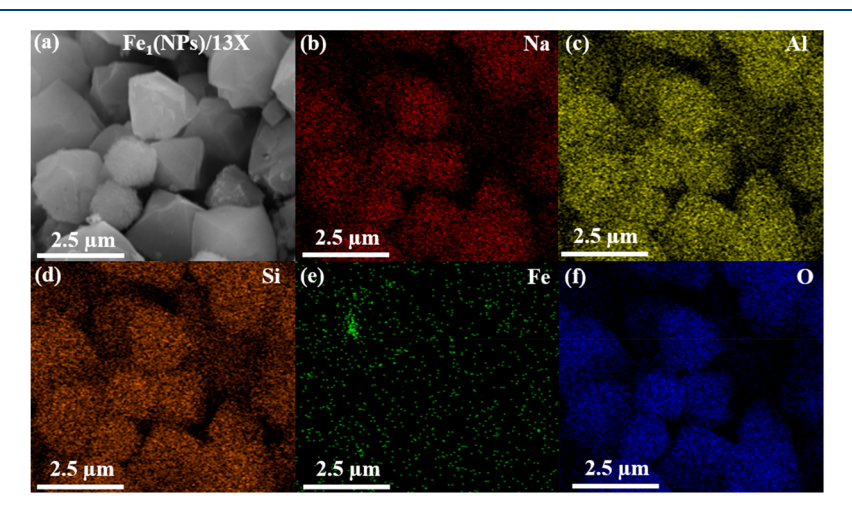


Figure 2. (a) SEM image of Fe₁(NPs)/13X and (b-f) the corresponding EDS mapping images for Na, Al, Si, Fe, and O elements.

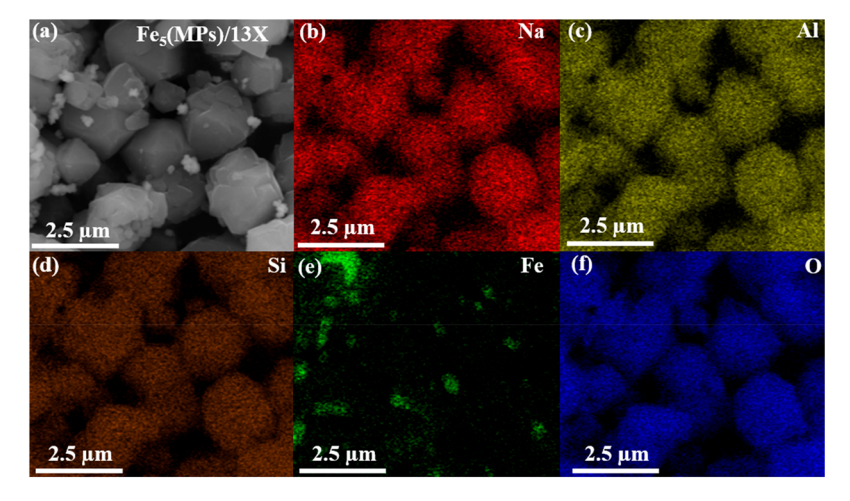


Figure 3. (a) SEM image of Fe₅(MPs)/13X and (b-f) the corresponding EDS mapping images for Na, Al, Si, Fe, and O elements.

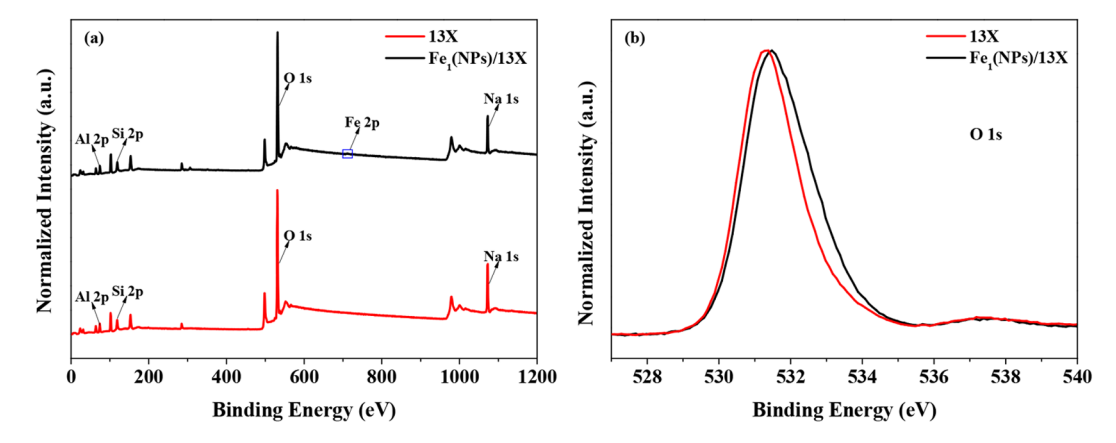


Figure 4. (a) XPS survey spectra and (b) high-resolution spectra of the O 1s for 13X and Fe₁(NPs)/13X.

of the Na, Al, Si, Fe, and O elements of the 13X and Fe_x/13X sorbents are presented in Figure S2a-e (13X), Figure 2a-f (Fe₁(NPs)/13X), Figure 3a-f (Fe₅(MPs)/13X), and Figure S3a-f (Fe₅(Ion)/13X), respectively. The particles of 13Xdepicted an octahedral structure with a nearly round shape, which was consistent with the typical crystalline state of 13X. 36,37 The synthesized Fe₁(NPs)/13X and Fe₅(Ion)/13X sorbents exhibited remarkable crystallinity, indicating of uniform distribution of Fe species within the 13X crystals (Figure 2 and Figure S3). The interaction between the Fe species and the 13X crystal is clearly evident from the images, confirming their successful incorporation within the crystal structure. In the case of Fe₅(MPs)/13X, where larger Fe particles were present, a distinct mode of interaction between Fe species and the 13X crystal was observed. These Fe particles appeared as separate entities, dispersed on the external surface of the 13X particles with the possibility of partial doping into the large pores, as evidenced by SEM images (Figure 3a) and EDS mapping results (Figure 3e). It can be concluded that Fe particles were doped only into the larger pores of 13X (and on the external surface), thereby blocking the micropores, while partially obstructing the meso-macropores. The results also implied that the 1 wt % NPs and 5 wt % ion-exchanged Fe species are more attracted to the interplanar of the large pores. Furthermore, it is anticipated that the integration of Fe₁ into the 13X framework in Fe₁(NPs)/13X can lead to the contraction of the micropore channels, thereby enhancing the molecular sieving effect and improving the selectivity

toward C_2H_4 with smaller kinetic diameter. For example, Xiang et al.³¹ studied the impact of Fe doping on CO_2/N_2 separation over 13X zeolite and reported that the introduction of Fe narrows the micropore channels and allows CO_2 with smaller kinetic diameter to penetrate, while impeding the entry of relatively larger N_2 molecules.

To verify the oxidation state in which Fe species exist in Fe₁(NPs)/13X, the surface of the material was analyzed by XPS and compared to that of pristine 13X. The XPS spectra of both materials showed the existence of Si 2p, Al 2p, O 1s, and Na 1s, implying that the 13X structure was preserved in the composite (Figure 4a). The characteristic peak of Fe 2p at 711.48 eV was attributed to the Fe 2p_{1/2} of Fe³⁺, which is consistent with the literature. These findings demonstrate that the Fe species in Fe₁(NPs)/13X exist in the isolated Fe³⁺ form within the 13X zeolite framework. Furthermore, together with the EDS mapping results, it was found that the active iron species mainly exist in the form of Fe³⁺, with a small amount of Fe³⁺ in the large pore channels. This suggested that Fe3+ was doped onto the 13X framework, leading to an increase in electronegativity and a stronger absorption peak.³¹ This can be observed from a slight shift in the O 1s peak to a higher binding energy in Fe₁(NPs)/13X compared to that in 13X (Figure 4b).

The N_2 physisorption isotherms and PSD profiles of the 13X and $Fe_x/13X$ sorbents are depicted in Figure 5, and the corresponding textural properties are summarized in Table 1. The N_2 isotherms and PSD profiles of the Fe_2O_3 particles

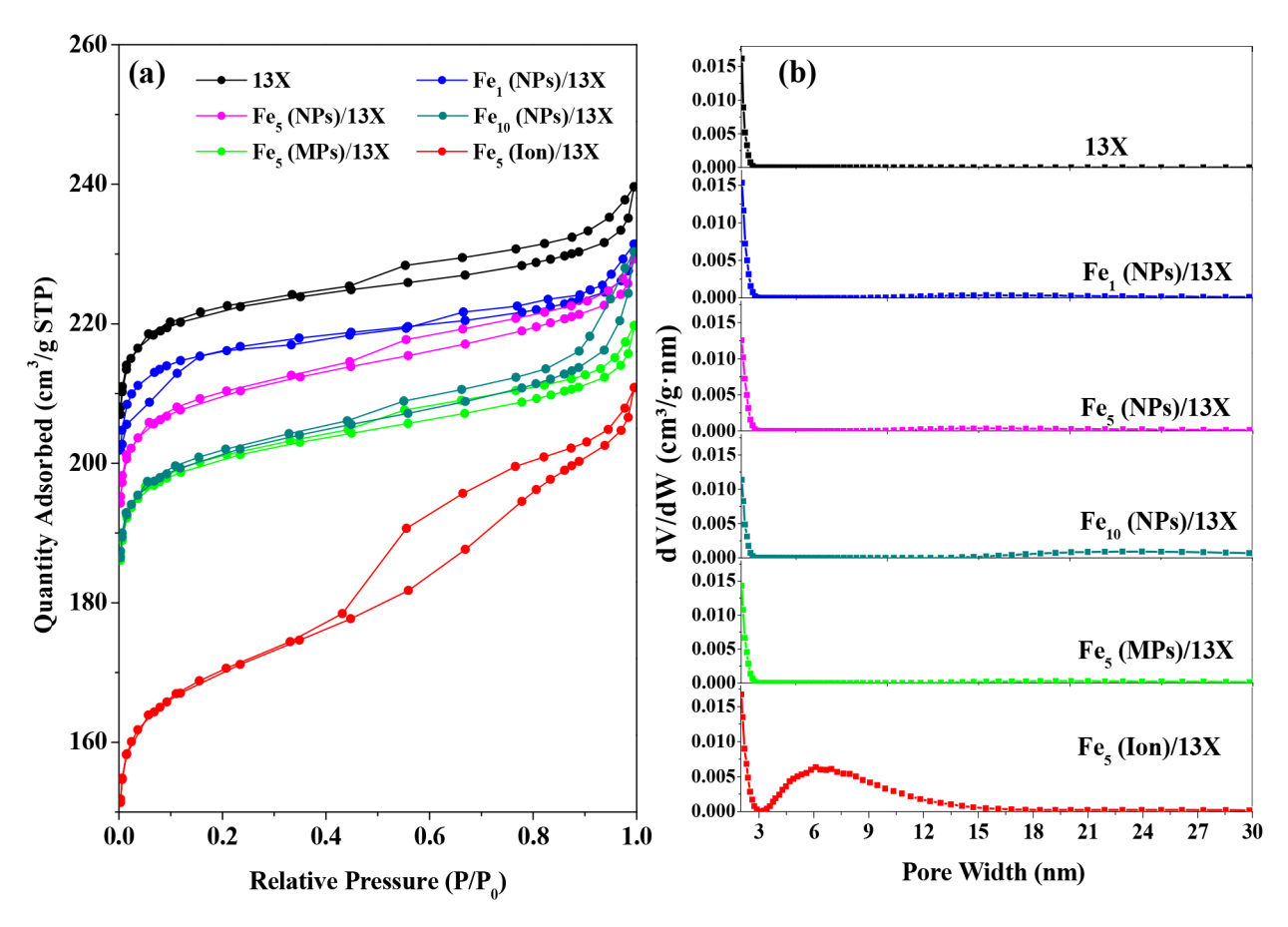


Figure 5. (a) N₂ physisorption isotherms and (b) PSD profiles of 13X and Fe_x/13X sorbents.

Table 1. Textural Properties of 13X and Fe_x/13X Sorbents

Sorbent	$\binom{S_{\rm BET}}{({\rm m}^2/{\rm g})}$	$V_{ m micro} \over ({ m cm}^3/{ m g})$	$\frac{V_{\mathrm{meso}}}{(\mathrm{cm}^3/\mathrm{g})}$	$d_{\rm p}$ (nm)
13X	892	0.310	0.046	2.0, 2.3, 2.4, 2.5, 2.6
Fe ₁ (NPs)/ 13X	824	0.300	0.052	2.0, 2.1, 2.4, 2.5, 2.6
Fe ₅ (NPs)/ 13X	815	0.294	0.059	2.0, 2.1, 2.4, 2.5, 2.6
Fe ₁₀ (NPs)/ 13X	780	0.289	0.064	2.2, 2.5, 2.7, 3.1, 3.8
$Fe_5(MPs)/$ $13X$	768	0.282	0.058	2.2, 2.5, 2.7, 3.1, 3.8
Fe ₅ (Ion)/13X	660	0.225	0.101	2.2, 2.5, 2.7, 3.1, 3.8

(NPs and MPs) are also shown in Figure S1, Supporting Information, which clearly show Type II isotherms for both ${\rm Fe_2O_3}$ particle sizes, with essentially no micropore volume. However, ${\rm Fe_2O_3}$ (NPs) displayed higher ${\rm N_2}$ uptake at higher P/P_0 ranges, indicating their higher degree of mesoporosity than ${\rm Fe_2O_3}$ (MPs). On the other hand, the 13X and ${\rm Fe_x}/13X$ sorbents displayed Type I isotherms with a narrow hysteresis loop (Type IV), indicative of their predominant microporous structures with some degree of mesoporosity. The mesopore volume was noted to increase upon Fe doping in all ${\rm Fe_x}/13X$ composites, as shown in Figure 5b and Table 1. The change in PSD profiles can stem from different sources: (i) Fe particles doped onto the 13X zeolite framework can occupy/obstruct some of the micropores, thereby reducing the available micropore volume. (ii) The introduction of Fe

particles into the zeolite can also lead to the formation of mesopores or enlargement of existing mesopores due to Fe particles agglomeration (e.g., at higher Fe loadings or larger particle sizes), which may result in the creation of larger pores. (iii) Fe particles can induce structural changes in the zeolite framework due to molecular interactions, as evident from the EDS mapping images for Fe₁(NPs)/13X and Fe₅(Ion)/13X, and XPS for Fe₁(NPs)/13X, thereby leading to the formation of mesopores and confinement of micropores. It was noted that for Fe₅(Ion)/13X, the PSD profile was distinct from that of the other Fe_x/13X samples, probably due to its different method of synthesis.

3.2. Unary Adsorption Isotherms. The unary equilibrium adsorption isotherms of C₂H₆, C₂H₄, CH₄, and H₂ were obtained at 25 °C and over the pressure range 0−1 bar, as depicted in Figure 6a-d. The bare 13X displayed higher affinity toward C2H4 than C2H6 and much lower affinity toward CH₄ and H₂. Also, as apparent, the shape of the isotherms of C₂H₆ and C₂H₄ for all Fe_x-doped sorbents resembled that of the parent 13X isotherms with a slight enhancement in equilibrium adsorption capacity for Fe₁(NPs)/13X, displaying a steep increase in the uptake at low pressures, followed by a gradual increase at higher pressures, whereas CH₄ and H₂ isotherms showed a gradual increase over the entire pressure range without any indications to reach saturation. Notably, the amounts of C_2H_6 , C_2H_4 , CH_4 , and H₂ adsorbed were reduced as the Fe_x loading in the Fe_x/ 13X was increased above 1 wt %, particularly significant uptake reduction was observed for Fe₅(Ion)/13X. The reduction in C₂H₆, C₂H₄, CH₄, and H₂ equilibrium capacities and the

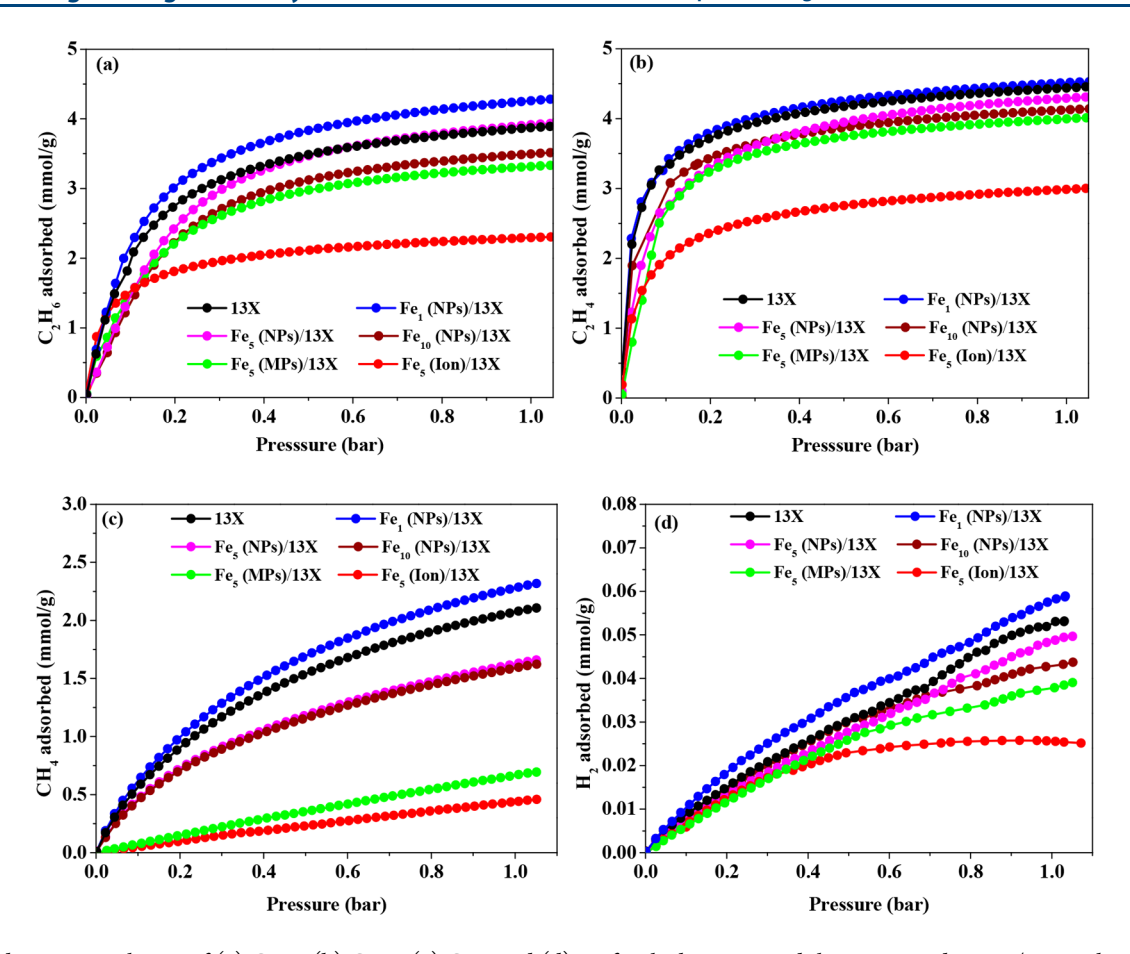


Figure 6. Adsorption isotherms of (a) C_2H_{4} , (b) C_2H_{4} , (c) CH_{4} , and (d) H_2 for the bare 13X and the corresponding $Fe_x/13X$ sorbents at 25 °C.

change in the shape of isotherms with increasing the loading/ or particle size of Fe_x could be attributed to the reduction in porosity and BET area. Nevertheless, the enhancement in equilibrium uptake of pure gases over $Fe_1(NPs)/13X$ despite its lower surface area can be attributed to the electronegativity enhancement over the sorbent surface, as discussed before. 44,45

The bare sorbent showed an equilibrium capacity of 3.94 mmol/g for C_2H_6 and 4.45 mmol/g for C_2H_4 at 1 bar, whereas $Fe_1(NPs)/13X$, $Fe_5(NPs)/13X$, $Fe_5(NPs)/13X$, $Fe_5(NPs)/13X$, $Fe_5(NPs)/13X$, and $Fe_5(Ion)/13X$ achieved capacities of 4.29, 3.90, 3.52, 3.30, and 2.30 mmol/g, respectively, for C_2H_6 and 4.52, 4.31, 4.13, 4.01, and 3.00 mmol/g for C_2H_4 , respectively, as presented in Figure 6a-b. On the other hand, the adsorption capacities of CH_4 and H_2 were much lower than C_2H_4 . The results indicate that these sorbents are selective toward C_2H_4 over C_2H_6 , and more selective over CH_4 and H_2 .

3.3. Breakthrough Experiments. 3.3.1. Effect of Particle Size at Fixed Fe_x Composition. To assess the separation capability of the developed sorbents, breakthrough experiments were performed by using a binary gas mixture of C_2H_6 and C_2H_4 at equimolar concentrations, and the dynamic concentration profiles for the bare 13X and Fe_x -doped 13X sorbents were collected, as illustrated in Figure 7. It is worth noting here that the definition of the term "equimolar" refers to C_2H_6 and C_2H_4 species and excludes Ar. In agreement with their 13X parent, all of the Fe_x -doped sorbents displayed preferential adsorption of C_2H_4 over C_2H_6 with high separation efficiency. From the concentration fronts, the overshoot in the wavefront of C_2H_6 was caused by the C_2H_4 breakthrough from the bed outlet, whose magnitude was

significant for 13X, and slightly reduced for Fe₅(NPs)/13X and Fe₅(MPs)/13X while significantly reduced for Fe₅(Ion)/13X (Figure 7a-d). The weaker adsorbate molecules of C₂H₆ were displaced by the stronger C₂H₄ molecules which resulted in the overshoot above the relative concentration of $C_i/C_0 = 1.40,46,47$ When C₂H₄ approached the end of the column, binary saturation was achieved, and both gases returned to their molar feed compositions. Since the uptakes of C₂H₆ and C₂H₄ were lower over Fe₅(Ion)/13X than over other sorbents, the shape of the roll-up or overshoot in the C₂H₆ concentration front was clearly different over this material with less sharpness relative to that over the other sorbents. The lower dynamic adsorption capacity of C_2H_6 (at $t_{ads,95\%}$) compared to its equilibrium capacity can be ascribed to the competitive adsorption of C₂H₆ and C_2H_4 in the binary system (Table 2). From the breakthrough profiles shown in Figure 7, it can be deduced that although doping Fe₅ NPs had a negligible effect on the adsorption performance of 13X, increasing the particle size (e.g., to MPs) or changing the synthesis method (e.g., ion exchange) at fixed Fex composition resulted in deteriorated adsorption performance of the composites relative to the pristine 13X.

3.3.2. Effect of Fe_x Composition at Fixed Particle Size. In the next step, we varied the composition of doped Fe_x NPs onto the 13X and assessed its impact on the separation performance of the composites. Fe_1 NPs, as present in $Fe_1(NPs)/13X$, demonstrated improvement in breakthrough time and adsorption capacity, as indicated in Figure 8a-b and Table 2. The introduction of Fe_1 into the 13X framework led to the confinement of the micropore channels, thereby

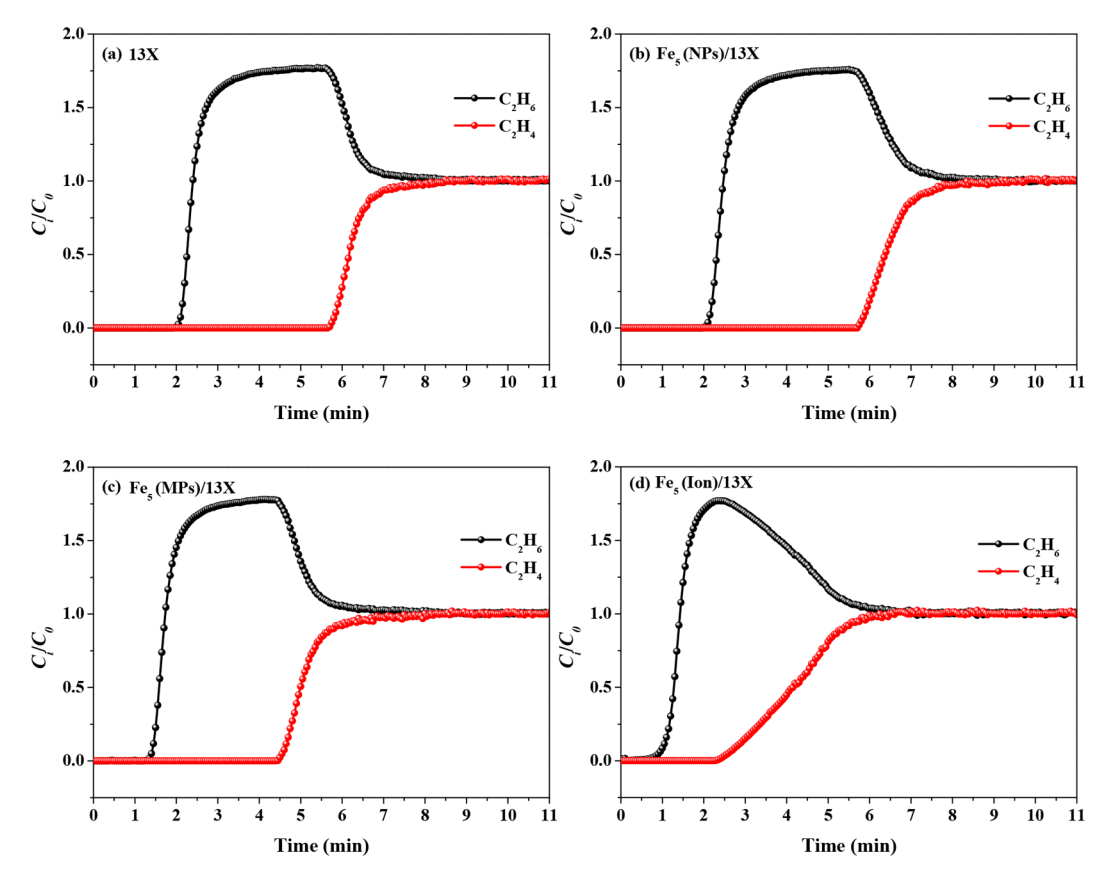


Figure 7. Dynamic concentration profiles for 50/50 vol % C_2H_6/C_2H_4 at 25 °C and 1 bar over (a) 13X, (b) $Fe_5(NPs)/13X$, (c) $Fe_5(MPs)/13X$, and (d) $Fe_5(Ion)/13X$.

Table 2. Dynamic Adsorption Data for Binary Runs at 25 °C and 1 bar for 13X and the Corresponding Fe,/13X Composites

Sorbent	$t_{\rm ads,5\%}$ (min)	$t_{ m ads,50\%}$ (min)	t _{ads,95%} (min)	Breakthrough width (min)	$q_{ads,5\%}$ (mmol/g)	$q_{\rm ads,50\%}~(\rm mmol/g)$	$q_{\rm ads,95\%}$ (mmol/g)
				C_2H_6			
13X	2.10	2.27	2.39	0.29	0.50	0.56	0.81
$Fe_1(NPs)/13X$	2.83	3.02	3.12	0.29	0.56	0.85	0.84
$Fe_5(NPs)/13X$	2.11	2.32	2.47	0.36	0.51	0.74	0.82
$Fe_{10}(NPs)/13X$	1.31	1.48	1.63	0.32	0.50	0.70	0.79
$Fe_5(MPs)/13X$	1.40	1.59	1.73	0.33	0.44	0.50	0.77
Fe ₅ (Ion)/13X	0.92	1.32	1.42	0.50	0.44	0.56	0.72
				C_2H_4			
13X	5.77	6.18	7.12	1.35	2.79	2.80	3.17
$Fe_1(NPs)/13X$	6.85	7.2	8.65	1.80	2.89	2.98	3.43
$Fe_5(NPs)/13X$	5.82	6.38	7.51	1.69	2.79	2.82	3.28
$Fe_{10}(NPs)/13X$	4.80	5.28	6.85	2.05	2.70	2.73	3.15
$Fe_5(MPs)/13X$	4.55	4.99	6.24	1.69	2.43	2.46	2.99
$Fe_5(Ion)/13X$	2.48	3.65	5.42	2.94	1.66	1.69	2.83

enhancing the molecular sieving effect and favoring C_2H_4 selectivity. C_2H_4 , with a smaller kinetic diameter compared to C_2H_6 (4.163 Å vs 4.443 Å), ⁴⁸ effectively penetrated into the pores of 13X, whereas C_2H_6 , with a larger kinetic diameter, was excluded from the smaller pores of 13X. ^{13,16} Additionally, the presence of Fe particles in the Fe₁(NPs)/13X composite, predominantly in the form of Fe³⁺, promoted stronger interactions between C_2H_4 and the surface through van der Waals (vdW) forces (i.e., π -bond interactions and dipole/quadrupole moments). On the other hand, in the case of Fe₁₀(NPs)/13X, the separation efficiency declined due to the particles agglomeration and pore blockage. Comparison of the binary adsorption performance of Fe_x-doped 13X composites

rendered $Fe_1(NPs)/13X$ as the best performing sorbent for further cyclic experiments. To better characterize the adsorption stability of this material, five cyclic runs were performed and the experimental results are shown in Figure 9. $Fe_1(NPs)/13X$ sorbent displayed laudable separation performance after the fifth cycle, indicating that this Fe_x -doped sorbent is a promising candidate for actual C_2H_6/C_2H_4 separation.

The measured equilibrium adsorption data were fitted with Sips model to determine the IAST selectivities as this model was found to adequately describe most of the adsorption types. As shown in Figures S4–S9, the Sips model satisfactorily described the $\rm C_2H_4$ and $\rm C_2H_6$ uptakes, and the isotherm model parameters are reported in Tables S4–S9,

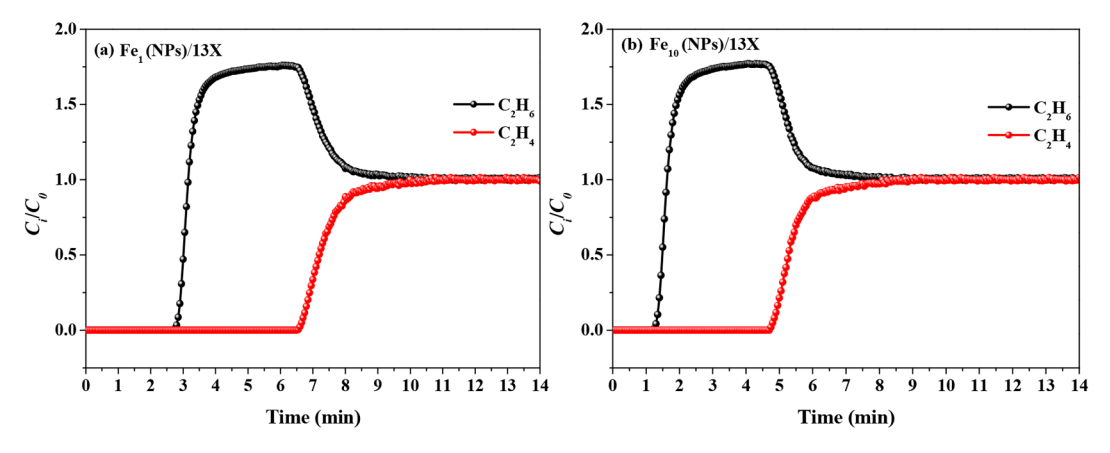


Figure 8. Dynamic concentration profiles for 50/50 vol % C₂H₆/C₂H₄ at 25 °C and 1 bar over (a) Fe₁(NPs)/13X and (b) Fe₁₀(NPs)/13X.

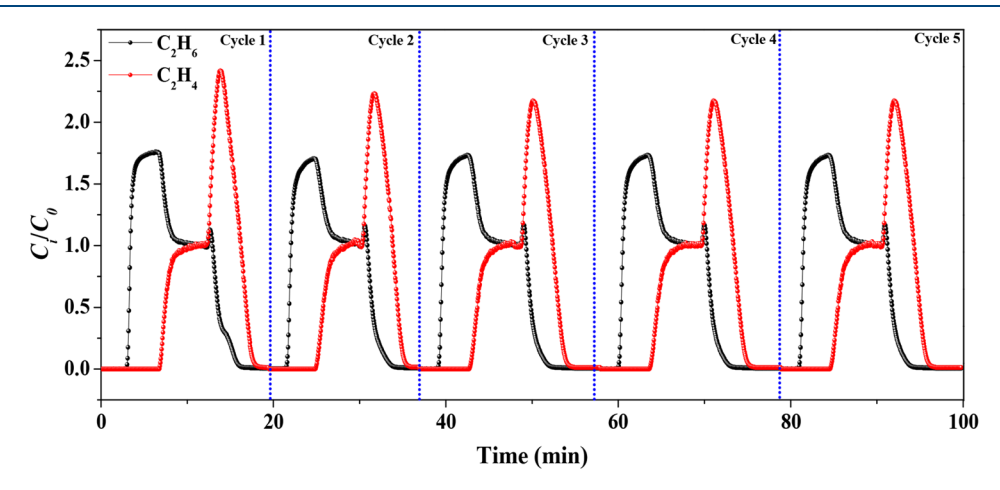


Figure 9. Cyclic breakthrough profiles for 50/50 vol % C₂H₆/C₂H₄ at 25 °C and 1 bar over Fe₁(NPs)/13X.

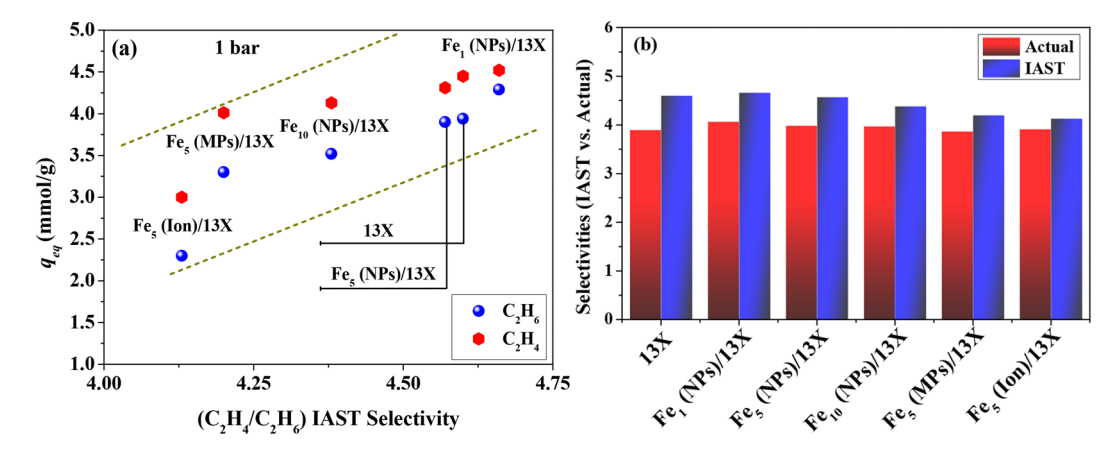


Figure 10. (a) IAST selectivity vs equilibrium adsorption capacity (mmol/g) of C_2H_6 and C_2H_4 obtained for 13X and corresponding $Fe_x/13X$ at 25 °C and 1 bar and (b) comparison between the IAST and actual C_2H_4/C_2H_6 selectivities.

Supporting Information. The IAST C_2H_4/C_2H_6 selectivities as a function of the equilibrium capacities (q_{eq}) are illustrated in Figure 10a-b. The $Fe_x/13X$ composites exhibited favorable C_2H_4 selectivity like their parent zeolite, but the C_2H_4 and C_2H_6 equilibrium uptakes were reduced with an increase in the Fe_x content. For example, while the C_2H_4 and C_2H_6 equilibrium uptakes of the bare 13X were 4.45 and 3.94 mmol/g, they were reduced to 3.0 and 2.3 mmol/g for $Fe_5(Ion)/13X$, respectively. However, the $Fe_1(NPs)/13X$ displayed higher equilibrium adsorption capacity and selectiv-

ity than the bare 13X. This improvement can be attributed to the narrowing of micropores resulting from the incorporation of Fe₁(NPs), which in turn promotes the molecular sieving effect, improves C_2H_4 selectivity due to its smaller size, and increases interaction between C_2H_4 and the sorbent via vdW forces mediated by Fe³⁺ species, as discussed earlier.^{7,31} Upon increasing the loading of Fe_x to > 1 wt %, the selectivity experienced a slightly decreasing trend, which ranged between 4.6 and 4.13. It can be concluded that increasing the Fe_x composition above 1 wt % impacted the uptakes of both C_2H_4

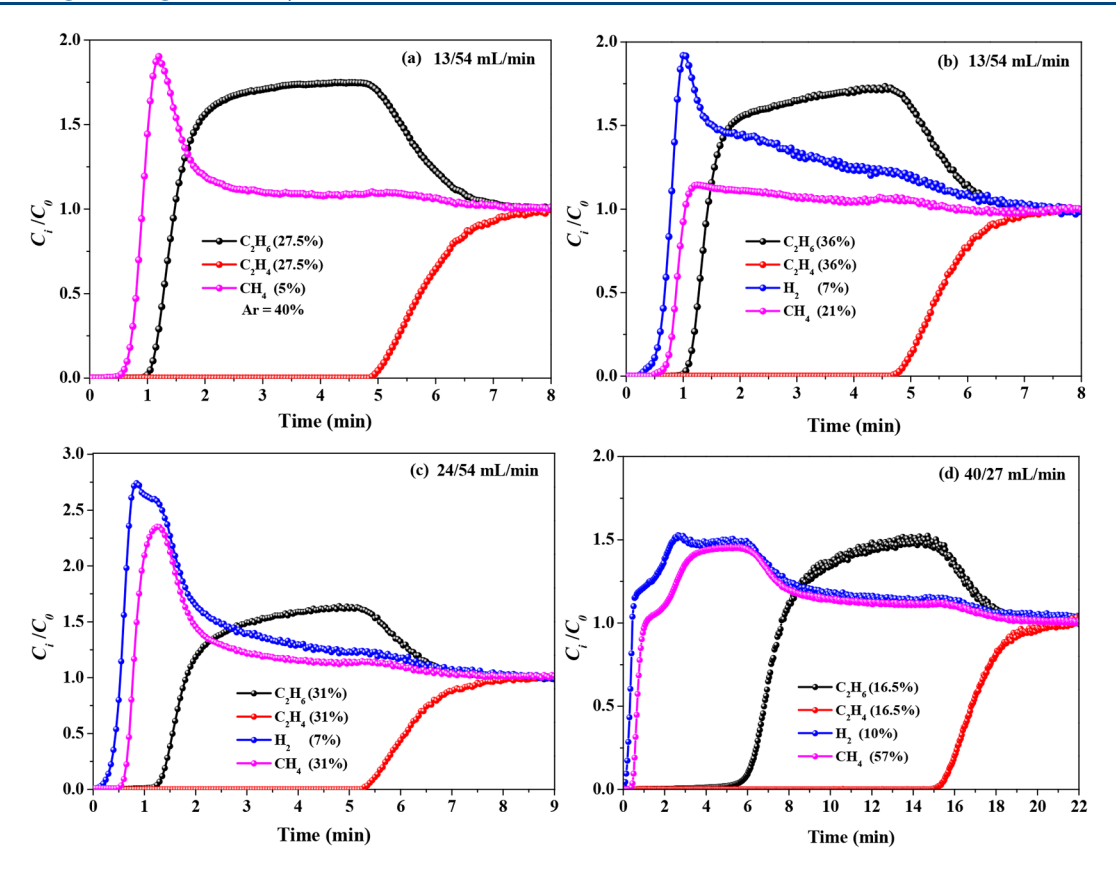


Figure 11. Dynamic concentration profiles at different feed flow rates for ternary and multicomponent gas mixtures: (a) 13/54 mL/min ternary $(CH_4/C_2H_6-C_2H_4)$, (b) 13/54 mL/min multicomponent $(H_2-CH_4/C_2H_6-C_2H_4)$, (c) 24/54 mL/min multicomponent $(H_2-CH_4/C_2H_6-C_2H_4)$, and (d) 40/27 mL/min multicomponent $(H_2-CH_4/C_2H_6-C_2H_4)$ at 25 °C and 1 bar over Fe₁ (NPs)/13X.

and C_2H_6 , resulting in roughly constant selectivities from both the theoretical and the actual trials over all Fe_x/13X sorbents, as demonstrated in Figure 10a-b.

3.4. Ternary and Multicomponent Breakthrough Experiments. After investigating the performance of $\mathrm{Fe_1(NPs)/13X}$ in binary $\mathrm{C_2H_6/C_2H_4}$ separation runs, we also aimed at further assessing its adsorption behavior in ternary and multicomponent flow streams under identical conditions, and the corresponding results are shown in Figure 11a-b and Table 3. It is worth noting that under specific

Table 3. Dynamic Adsorption Data for Binary, Ternary, and Multicomponent Runs at 25 °C and 1 bar for Fe₁(NPs)/13X

	Gas mixture	Gases			
Parameter	C ₂ H ₆ /C ₂ H ₄ /CH ₄ /H ₂	C_2H_6	C_2H_4	CH ₄	H_2
$q_{\rm ads,95\%}$ (mmol/g)	35.5/35.5/-/-	0.84	3.43	-	-
	27.5/27.5/5/-	0.83	3.38	0.05	-
	36/36/21/7	0.82	3.34	0.21	0.01
	31/31/31/7	0.81	3.30	0.26	0.01
	16.5/16.5/57/10	1.72	4.20	0.25	0.02

conditions, such as reaction temperature and catalyst type, methane as a heavy component can be produced at both low and high concentrations, particularly during the process of ethane dehydrogenation. As a result, it becomes crucial to investigate the presence and abundance of methane at varying concentrations when separating ethane and ethylene. In order to accomplish this, the methane concentration was deliberately

varied, ranging from a low concentration, as observed in the ternary gas mixture (Figure 11a) to a high concentration, as observed in the multicomponent gas mixture (Figure 11d).

The sorbent displayed comparable adsorption performance in the ternary and multicomponent streams to that in the binary stream. However, the C_2H_4 breakthrough time $(t_{ads,5\%})$ was reduced in the ternary and multicomponent runs relative to the binary experiment, from 6.85 min to 5.24 and 5.10 min, respectively. This reduction in the breakthrough time is indicative of competitive adsorption effects that resulted in kicking-out the gases earlier, or in other words, resulted in lower adsorption capacity in the presence of other impurities. The effect of the total flow rate on the multicomponent concentration profiles was also investigated by conducting breakthrough experiments at different feed flow rates, as shown in Figure 11c-d. What can be inferred from these profiles is that upon increasing the inlet flow rate, the $t_{ads,5\%}$ decreased for all gases, which was expected due to the shortened residence time. Moreover, analyzing the shape and width of the breakthrough profiles revealed that as the flow rate increased for the impurity gases (CH₄ and H₂), as in Figure 11b-c, their wavefronts became sharper, whereas no obvious changes in the wavefronts of C₂H₆ and C₂H₄ were noted, which was also expected as the flow rate was only increased for H2 and CH4 (from 13 to 24 mL/min). The roll-up area for H_2 (above C_i/C_0 = 1) was notably larger than the adsorbed area (below C_i/C_0 = 1) and such a difference can be attributed to the strong adsorption and long mass transfer zones (MTZs) of C₂H₆ and C₂H₄, causing rapid desorption of weakly-adsorbed species at the initial part of the column. In contrast, CH₄ and H₂ had

narrower MTZs, resulting in a more uniform advancement along the column. The MTZs of CH₄/H₂ continued to progress through subsequent column slices, gradually desorbing while being displaced by C2H6/C2H4. Although saturation of CH₄/H₂ was detected early on, a significant portion can be readsorbed in the remaining column. However, these dynamics are not fully captured by the graphs, potentially leading to discrepancies in calculated adsorption areas. The competition between species is most intense at the start of the process but decreases as the wider MTZ progresses. Relative concentrations remain relatively constant until the final phase, where they gradually return to their initial concentration, is attained. While it is uncommon for the desorption area to exceed the adsorption area, as seen with H₂ (Figure 11b-c), the total mass balance shows that the sum of adsorption areas exceeds the sum of desorption areas. This indicates that additional factors, such as flow differences, may impact the mass balance as well. Due to the lack of a proper premixing unit prior to the adsorption column in our setup, a pressure gradient can build up which can cause a delay in retention time for the components with lower flow rates (e.g., CH₄ and H₂), followed by a sudden surge through the column. As a result, these species exhibit a sharp overshoot with a larger desorption area. Interestingly, the actual selectivity values of C_2H_4/C_2H_6 were noted to be constant at 4.07, while the C₂H₄/ $(C_2H_6+CH_4+H_2)$ selectivities were reduced (see Table 4).

Table 4. Selectivity Values of C_2H_4/C_2H_6 and $C_2H_4/(C_2H_6+CH_4+H_2)$ for Binary, Ternary, and Multicomponent Runs at 25 °C and 1 bar for $Fe_1(NPs)/13X$

	Selectivity (S)			
Gas mixture $(C_2H_6/C_2H_4/CH_4/H_2)$	C_2H_4/C_2H_6	$C_2H_4/$ $(C_2H_6+CH_4+H_2)$		
35.5/35.5/-/-	4.10	4.10		
27.5/27.5/5/-	4.07	3.84		
36/36/21/7	4.07	3.20		
31/31/31/7	4.07	3.05		
16.5/16.5/57/10	2.44	2.11		

For instance, the $C_2H_4/(C_2H_6+CH_4+H_2)$ selectivity was estimated to be 3.84 in Figure 11a, which was reduced to 3.05 upon increasing the flow rate due to competitive adsorption effects (Figure 11c).

The same trends and effects could be realized for CH₄ and H₂ in Figure 11d, as the flow rate of CH₄ and H₂ kept increasing to 40 mL/min, while different trends were noted for C_2H_6 and C_2H_4 as their flow rate reduced to 27 mL/min. Despite the high flow rates of CH₄ and H₂, their adsorption capacities remained roughly unchanged, probably due to a reduction in contact time for CH₄ and H₂ adsorbates, even though their concentrations increased. However, in the case of C₂H₆ and C₂H₄ adsorption, different trend was observed when the flow rate decreased to 27 mL/min. The $t_{ads.5\%}$ delayed significantly for C₂H₆ and C₂H₄, and consequently, the pseudo-equilibrium capacities reached 1.72 and 4.20 mmol/g for C₂H₆ and C₂H₄, respectively, as compared to 0.81 and 3.30 mmol/g in Figure 11c. The wavefronts of C_2H_6 and C_2H_4 were also broadened, indicating that the contact time of the adsorbates increased at a lower flow rate as the overall flow rate was reduced from 78 to 67 mL/min. However, increasing the adsorption capacity of C₂H₆ and C₂H₄ led to reduced C_2H_4/C_2H_6 selectivity, as shown in Table 4.

3.5. Kinetic Analysis of Multicomponent Separation.

To characterize the difference in kinetic behavior of the Fe₁(NPs)/13X sorbent across the three gas mixtures (binary, ternary, multicomponent), parameters estimation was carried out following a methodology described in our prior work.⁴⁹ As evident from Figure 12a-d, all fittings achieved R² values greater than 0.99, indicating that the estimated parametric data well-represented the experimental data sets. The kinetic constants were calculated using curve fitting in combination with eqs S4-S22, reported in the Supporting Information, and the data are summarized in Table 5. Analyzing the data revealed a smaller pore mass transfer (k_p) than the film transport (k_f) for all species, by roughly one order of magnitude, indicating that the overall transport in all three mixtures is controlled primarily by the transport through the pores of the composite, in agreement with previous studies. $^{34,47,50-52}$ The values of $k_{\rm LDF}$ provide additional insight into this discussion. $k_{\rm LDF}$ represents the rate of diffusion through the zeolite's interconnected channels, which is influenced by both the pore structure and adsorbateadsorbent interactions.⁵³ The higher values of k_{LDF} for C_2H_4 compared to those for C2H6 suggested that C2H4 has a higher diffusion rate through the pores, which can be attributed to its smaller size and stronger interaction with the pore surface. However, the presence of other impurity gases such as CH₄ and H₂ has an impact on the adsorption kinetics of C₂H₄ on the 13X zeolite. This discrepancy can be explained by the adsorption mechanism of C2H4 over 13X. C2H4, being smaller in molecular diameter than C₂H₆, can diffuse more easily through the small pores of the zeolite. Once C₂H₄ penetrates and fills the pores, it is attracted to the pore surface via vdW forces. However, this adsorption phenomenon can be perturbed in ternary and multicomponent mixtures by competitive gas adsorption effects, leading to a reduction in the adsorption kinetics of C₂H₄, particularly in terms of pore transport. This effect is evident from the data presented in

Moving onto the transport of the gases in the three different gas mixtures, the effective diffusion rates corresponded well with the dynamic results in Table 5. Namely, the effective diffusivity (D_{eff}) of C₂H₆ and C₂H₄ reduced by 5.55 and 37.56% as impurities were added into the feed stream, with values ranked in the order of binary > ternary > multicomponent. For CH_4 , on the other hand, the $D_{\rm eff}$ value was higher in the multicomponent mixture than in the ternary feed, which was attributed to its higher concentration in the multicomponent feed. It should be noted here that although all gases exhibited the same order of magnitude of D_{eff} , the rankings of the individual gases in the multicomponent gas mixture followed: $H_2 > CH_4 > C_2H_4 > C_2H_6$. The obtained rankings did correspond to H₂ and CH₄, breaking through first and second. Moreover, CH₄ consistently broke through before C₂H₆ and C₂H₄ even though the CH₄ had equivalent or higher effective diffusivity due to its lower adsorption capacity. Such effects can be attributed to the heavier C2H6 and C2H4 displacing the lighter H₂ and CH₄ adsorbates. In other words, the heavier species can facilitate exclusion of the lighter contaminants, further indicating that the order at which multiple species break through the column in multicomponent mixtures is not only depended on adsorbate-adsorbent interactions, but also on the effective diffusivity of each adsorbate, which are both impacted by competitive or cooperative adsorption effects. In Figure 12d, a comparison

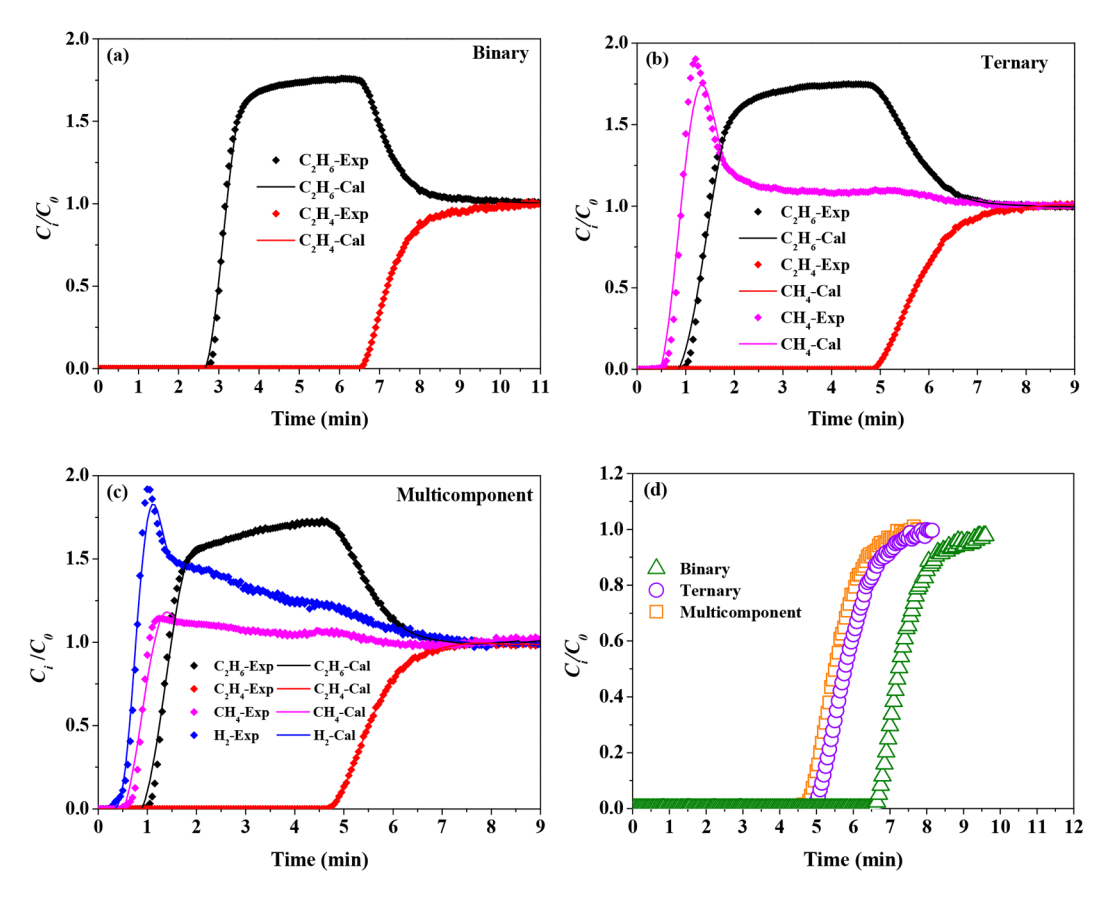


Figure 12. (a–c) Fitted breakthrough profiles for binary, ternary, and multicomponent runs at 25 $^{\circ}$ C and 1 bar for Fe₁(NPs)/13X sorbent, and (d) comparison between the wavefronts of C₂H₄ in binary, ternary, and multicomponent experiments.

Table 5. Mass Transfer Parameters for Fe₁(NPs)/13X at Different Gas Mixtures

Gas mixture	Gas	$k_{\rm LDF} \times 10^3 \ (\rm s^{-1})$	$k_{\rm f} \times 10 \; ({\rm cm/s})$	$k_{\rm p} \times 10^2 \; ({\rm cm/s})$	$D_{\rm eff} \times 10^5 \ ({\rm cm}^2/{\rm s})$	$k_{\text{overall}} \times 10^2 \text{ (s}^{-1}\text{)}$
Binary	C_2H_6	6.33	3.56	2.68	2.70	2.32
	C_2H_4	7.83	3.51	4.07	4.10	3.29
Ternary	C_2H_6	5.67	3.70	2.59	2.59	2.18
	C_2H_4	6.00	3.60	3.86	3.86	3.01
	CH_4	4.33	3.90	0.27	0.26	0.26
Multicomponent	C_2H_6	4.67	3.60	2.68	2.55	2.30
	C_2H_4	5.50	3.60	2.68	2.56	2.32
	CH_4	3.67	4.40	2.65	2.64	2.28
	H_2	3.33	12.5	4.92	4.99	3.05

between the wavefronts of C_2H_4 in binary, ternary, and multicomponent trials is presented to better demonstrate how the complexity of the mixture environment affects the dynamic separation of the $\text{Fe}_1(\text{NPs})/13X$ sorbent. What can be observed here is an apparent reduction in breakthrough time in the ternary and multicomponent runs relative to the binary system, which indicated the lower adsorption capacity due to the competitive effects when CH_4 was present. However, the presence of H_2 had a marginal effect on the separation behavior of the material.

4. CONCLUSIONS

In this work, we evaluated the ethylene purification performance of Fe_x -doped 13X composite sorbents under binary, ternary, and multicomponent gas mixtures. Our results

indicated that doping nanoparticles of Fe_2O_3 onto zeolite 13X, as in $Fe_1(NPs)/13X$, gives rise to enhanced adsorption capacity and selectivity, as a result of improved surface electronic transfers that could boost the π -ion interactions between the unsaturated double bond in C_2H_4 and the $Fe_1(NPs)/13X$'s surface active sites. Furthermore, the introduction of Fe_1 into the 13X framework led to the constriction of micropore channels, thereby enhancing the molecular sieving effect and favoring C_2H_4 selectivity. However, the surface area and microporosity of the doped sorbents were found to reduce drastically upon doping Fe_2O_3 onto 13X, and much reduction was observed for composites with higher content or larger particle size of Fe_x compared to the bare zeolite. Using a gas mixture of $C_2H_6/C_2H_4/CH_4/H_2$ with 36/36/21/7 volumetric composition, the selectivity for

 $C_2H_4/(C_2H_6+CH_4+H_2)$ over $Fe_1(NPs)/13X$ was found to be 3.20, which was smaller than C_2H_4/C_2H_6 selectivity values in ternary and binary mixtures (ca. 4.07 and 4.10, respectively). Through modeling of concentration fronts, the overall transport for all three gas mixtures was found to be controlled by the pore diffusion through the solid particles. Overall, this study provides a comprehensive analysis of adsorption equilibria and dynamics of light hydrocarbons separation over Fe_x -doped 13X sorbents under various feed conditions.

ASSOCIATED CONTENT

Supporting Information

The Supporting Information is available free of charge at https://pubs.acs.org/doi/10.1021/acs.iecr.3c00620.

Materials characterization included the determination of the BET surface area and pore size distribution of iron oxide nanoparticles and microparticles; elemental analysis using ICP-MS, and SEM images of the developed sorbents; adsorption isotherms; physical properties of gases; bed porosity calculations; mass balance equations for experimental data fitting; molecular diffusivity calculations in binary, ternary, and multicomponent gas mixtures (PDF)

AUTHOR INFORMATION

Corresponding Author

Fateme Rezaei — Linda and Bipin Doshi Department of Chemical and Biochemical Engineering, Missouri University of Science and Technology, Rolla, Missouri 65409-1230, United States; orcid.org/0000-0002-4214-4235; Email: rezaeif@mst.edu

Authors

Khaled Baamran – Linda and Bipin Doshi Department of Chemical and Biochemical Engineering, Missouri University of Science and Technology, Rolla, Missouri 65409-1230, United States

Jimmy D. L. Moreno – Linda and Bipin Doshi Department of Chemical and Biochemical Engineering, Missouri University of Science and Technology, Rolla, Missouri 6S409-1230, United States

Ali A. Rownaghi — Department of Chemistry, Cleveland State University, Cleveland, Ohio 44115, United States;
orcid.org/0000-0001-5228-5624

Complete contact information is available at: https://pubs.acs.org/10.1021/acs.iecr.3c00620

Notes

The authors declare no competing financial interest.

ACKNOWLEDGMENTS

The authors acknowledge the materials research center (MRC) at Missouri University of Science and Technology for conducting SEM and XPS characterizations. The involvement of A.A.R. in this work was sponsored by the National Science Foundation (NSF CBET-2019350).

REFERENCES

(1) Mynko, O.; Amghizar, I.; Brown, D. J.; Chen, L.; Marin, G. B.; de Alvarenga, R. F.; Uslu, D. C.; Dewulf, J.; Van Geem, K. M. Reducing CO₂ Emissions of Existing Ethylene Plants: Evaluation of

- Different Revamp Strategies to Reduce Global CO₂ Emission by 100 Million Tonnes. *J. Clean. Prod.* **2022**, 362 (May), 132127.
- (2) Chen, C.-X.; Wei, Z.-W.; Pham, T.; Lan, P. C.; Zhang, L.; Forrest, K. A.; Chen, S.; Al-Enizi, A. M.; Nafady, A.; Su, C.-Y.; Ma, S. Nanospace Engineering of Metal—Organic Frameworks through Dynamic Spacer Installation of Multifunctionalities for Efficient Separation of Ethane from Ethane/Ethylene Mixtures. *Angew. Chemie Int. Ed.* **2021**, *60* (17), 9680–9685.
- (3) Kang, M.; Yoon, S.; Ga, S.; Kang, D. W.; Han, S.; Choe, J. H.; Kim, H.; Kim, D. W.; Chung, Y. G.; Hong, C. S. High-Throughput Discovery of $Ni(IN)_2$ for Ethane/Ethylene Separation. *Adv. Sci.* **2021**, 8 (11), 2004940.
- (4) Baamran, K.; Rownaghi, A. A.; Rezaei, F. Direct Synthesis of Ethylene and Hydrogen from CO₂ and Ethane over a Bifunctional Structured CaO/Cr₂O₃-V₂O₅/ZSM-5 Adsorbent/Catalyst Monolith. ACS Sustain. Chem. Eng. 2023, 11, 1006.
- (5) Lawson, S.; Baamran, K.; Newport, K.; Rezaei, F.; Rownaghi, A. Screening of Adsorbent/Catalyst Composite Monoliths for Carbon Capture-Utilization and Ethylene Production. *ACS Appl. Mater. Interfaces* **2021**, *13* (46), 55198–55207.
- (6) Lawson, S.; Baamran, K.; Newport, K.; Rezaei, F.; Rownaghi, A. A. Formulation and Processing of Dual Functional Adsorbent/ Catalyst Structured Monoliths Using an Additively Manufactured Contactor for Direct Capture/Conversion of CO₂ with Cogeneration of Ethylene. *Chem. Eng. J.* **2022**, 431, 133224.
- (7) Gong, Y.; Chen, C.; Lively, R. P.; Walton, K. S. Humid Ethylene/Ethane Separation on Ethylene-Selective Materials. *Ind. Eng. Chem. Res.* **2021**, *60*, 9940.
- (8) Schwach, P.; Pan, X.; Bao, X. Direct Conversion of Methane to Value-Added Chemicals over Heterogeneous Catalysts: Challenges and Prospects. *Chem. Rev.* **2017**, *117* (13), 8497–8520.
- (9) Adil, K.; Belmabkhout, Y.; Pillai, R. S.; Cadiau, A.; Bhatt, P. M.; Assen, A. H.; Maurin, G.; Eddaoudi, M. Gas/Vapour Separation Using Ultra-Microporous Metal—Organic Frameworks: Insights into the Structure/Separation Relationship. *Chem. Soc. Rev.* **2017**, *46* (11), 3402–3430.
- (10) Yang, Y.; Li, L.; Lin, R.-B.; Ye, Y.; Yao, Z.; Yang, L.; Xiang, F.; Chen, S.; Zhang, Z.; Xiang, S.; Chen, B. Ethylene/Ethane Separation in a Stable Hydrogen-Bonded Organic Framework through a Gating Mechanism. *Nat. Chem.* **2021**, *13* (10), 933–939.
- (11) Lyndon, R.; You, W.; Ma, Y.; Bacsa, J.; Gong, Y.; Stangland, E. E.; Walton, K. S.; Sholl, D. S.; Lively, R. P. Tuning the Structures of Metal—Organic Frameworks via a Mixed-Linker Strategy for Ethylene/Ethane Kinetic Separation. *Chem. Mater.* **2020**, 32 (9), 3715—3722
- (12) Li, L.; Lin, R.-B.; Krishna, R.; Li, H.; Xiang, S.; Wu, H.; Li, J.; Zhou, W.; Chen, B. Ethane/Ethylene Separation in a Metal-Organic Framework with Iron-Peroxo Sites. *Science* (80-.). **2018**, 362 (6413), 443–446.
- (13) Anwar, F.; Khaleel, M.; Wang, K.; Karanikolos, G. N. Selectivity Tuning of Adsorbents for Ethane/Ethylene Separation: A Review. *Ind. Eng. Chem. Res.* **2022**, *61* (34), 12269–12293.
- (14) Kim, J.; Lin, L.-C.; Martin, R. L.; Swisher, J. A.; Haranczyk, M.; Smit, B. Large-Scale Computational Screening of Zeolites for Ethane/Ethene Separation. *Langmuir* **2012**, 28 (32), 11914–11919.
- (15) Golipour, H.; Mokhtarani, B.; Mafi, M.; Moradi, A.; Godini, H. R. Experimental Measurement for Adsorption of Ethylene and Ethane Gases on Copper-Exchanged Zeolites 13X and 5A. *J. Chem. Eng. Data* **2020**, *65* (8), 3920–3932.
- (16) Narin, G.; Martins, V. F. D.; Campo, M.; Ribeiro, A. M.; Ferreira, A.; Santos, J. C.; Schumann, K.; Rodrigues, A. E. Light Olefins/Paraffins Separation with 13X Zeolite Binderless Beads. Sep. Purif. Technol. 2014, 133, 452–475.
- (17) Choi, B.-U.; Choi, D.-K.; Lee, Y.-W.; Lee, B.-K.; Kim, S.-H. Adsorption Equilibria of Methane, Ethane, Ethylene, Nitrogen, and Hydrogen onto Activated Carbon. *J. Chem. Eng. Data* **2003**, 48 (3), 603–607.
- (18) Liang, W.; Wu, Y.; Xiao, H.; Xiao, J.; Li, Y.; Li, Z. Ethane-Selective Carbon Composites CPDA@A-ACs with High Uptake and

- Its Enhanced Ethane/Ethylene Adsorption Selectivity. AIChE J. 2018, 64 (9), 3390–3399.
- (19) Wang, Z.; Yang, L.; Zhang, P.; Cui, J.; Chen, P.; Ding, Q.; Cui, X.; Xing, H. Highly Microporous Activated Carbons with Industrial Potential for Selective Adsorption of Ethane over Ethylene. *Ind. Eng. Chem. Res.* **2021**, *60* (36), 13301–13308.
- (20) Qazvini, O. T.; Babarao, R.; Shi, Z.-L.; Zhang, Y.-B.; Telfer, S. G. A Robust Ethane-Trapping Metal—Organic Framework with a High Capacity for Ethylene Purification. *J. Am. Chem. Soc.* **2019**, *141* (12), 5014—5020.
- (21) He, C.; Wang, Y.; Chen, Y.; Wang, X.; Yang, J.; Li, L.; Li, J. An Ethane-Favored Metal-Organic Framework with Tailored Pore Environment Used for Efficient Ethylene Separation. *Microporous Mesoporous Mater.* **2021**, 320, 111096.
- (22) Liao, P.-Q.; Zhang, W.-X.; Zhang, J.-P.; Chen, X.-M. Efficient Purification of Ethene by an Ethane-Trapping Metal-Organic Framework. *Nat. Commun.* **2015**, *6* (1), 1–9.
- (23) Freund, R.; Zaremba, O.; Arnauts, G.; Ameloot, R.; Skorupskii, G.; Dinca, M.; Bavykina, A.; Gascon, J.; Ejsmont, A.; Goscianska, J.; Kalmutzki, M.; Lachelt, U.; Ploetz, E.; Diercks, C. S.; Wuttke, S. The Current Status of MOF and COF Applications. *Angew. Chemie Int. Ed.* **2021**, *60* (45), 23975–24001.
- (24) Healy, C.; Patil, K. M.; Wilson, B. H.; Hermanspahn, L.; Harvey-Reid, N. C.; Howard, B. I.; Kleinjan, C.; Kolien, J.; Payet, F.; Telfer, S. G.; Kruger, P. E.; Bennett, T. D. The Thermal Stability of Metal-Organic Frameworks. *Coord. Chem. Rev.* **2020**, *419*, 213388.
- (25) Bazargan, M.; Ghaemi, F.; Amiri, A.; Mirzaei, M. Metal—Organic Framework-Based Sorbents in Analytical Sample Preparation. *Coord. Chem. Rev.* **2021**, 445, 214107.
- (26) Hyun, S. H.; Danner, R. P. Equilibrium Adsorption of Ethane, Ethylene, Isobutane, Carbon Dioxide, and Their Binary Mixtures on 13X Molecular Sieves. *J. Chem. Eng. Data* **1982**, *27* (2), 196–200.
- (27) Danner, R. P.; Choi, E. C. F. Mixture Adsorption Equilibria of Ethane and Ethylene on 13X Molecular Sieves. *Ind. Eng. Chem. Fundam.* **1978**, *17* (4), 248–253.
- (28) Baamran, K.; Rownaghi, A. A.; Rezaei, F. Magnetic-Induced Swing Adsorption over Iron Oxide/13X: Effects of Particle Size and Oxide Phase on Sorbent Regeneration in Ethylene/Ethane Separation. ACS Sustain. Chem. Eng. 2023, 11 (23), 8603–8614.
- (29) Popova, M.; Boycheva, S.; Lazarova, H.; Zgureva, D.; Lázár, K.; Szegedi, Á. VOC Oxidation and CO₂ Adsorption on Dual Adsorption/Catalytic System Based on Fly Ash Zeolites. *Catal. Today* **2020**, 357, 518–525.
- (30) Chanapattharapol, K. C.; Krachuamram, S.; Youngme, S. Study of CO₂ Adsorption on Iron Oxide Doped MCM-41. *Microporous Mesoporous Mater.* **2017**, 245, 8–15.
- (31) Xiang, X.; Guo, T.; Yin, Y.; Gao, Z.; Wang, Y.; Wang, R.; An, M.; Guo, Q.; Hu, X. High Adsorption Capacity Fe@13X Zeolite for Direct Air CO₂ Capture. *Ind. Eng. Chem. Res.* **2023**, *62* (12), 5420–5429
- (32) Sun, M.; Gu, Q.; Hanif, A.; Wang, T.; Shang, J. Transition Metal Cation-Exchanged SSZ-13 Zeolites for CO_2 Capture and Separation from N_2 . Chem. Eng. J. 2019, 370, 1450–1458.
- (33) Baamran, K.; Al-Naddaf, Q.; Lawson, S.; Ali Rownaghi, A.; Rezaei, F. Kinetic Process Assessment of H₂ Purification over Highly Porous Carbon Sorbents under Multicomponent Feed Conditions. Sep. Purif. Technol. **2023**, 306, 122695.
- (34) Wilkins, N. S.; Rajendran, A.; Farooq, S. Dynamic Column Breakthrough Experiments for Measurement of Adsorption Equilibrium and Kinetics. *Adsorption* **2021**, 27 (3), 397–422.
- (35) Rajendran, A.; Kariwala, V.; Farooq, S. Correction Procedures for Extra-Column Effects in Dynamic Column Breakthrough Experiments. *Chem. Eng. Sci.* **2008**, *63* (10), 2696–2706.
- (36) Chen, S. J.; Zhu, M.; Fu, Y.; Huang, Y. X.; Tao, Z. C.; Li, W. L. Using 13X, LiX, and LiPdAgX Zeolites for CO₂ Capture from Post-Combustion Flue Gas. *Appl. Energy* **2017**, *191*, 87–98.
- (37) Yang, F.; Wu, J.; Zhu, X.; Ge, T.; Wang, R. Enhanced Stability and Hydrophobicity of LiX@ZIF-8 Composite Synthesized Environ-

- mental Friendly for CO₂ Capture in Highly Humid Flue Gas. Chem. Eng. J. 2021, 410, 128322.
- (38) Zhou, Y.; Zhang, J.; Wang, L.; Cui, X.; Liu, X.; Wong, S. S.; An, H.; Yan, N.; Xie, J.; Yu, C.; Zhang, P.; Du, Y.; Xi, S.; Zheng, L.; Cao, X.; Wu, Y.; Wang, Y.; Wang, C.; Wen, H.; Chen, L.; Xing, H.; Wang, J. Self-Assembled Iron-Containing Mordenite Monolith for Carbon Dioxide Sieving. *Science* (80-.) 2021, 373 (6552), 315–320.
- (39) Chen, Z.; Liu, Q.; Guo, L.; Zhang, S.; Pang, L.; Guo, Y.; Li, T. The Promoting Mechanism of in Situ Zr Doping on the Hydrothermal Stability of Fe-SSZ-13 Catalyst for NH₃-SCR Reaction. *Appl. Catal. B Environ.* **2021**, 286, 119816.
- (40) Baamran, K.; Newport, K.; Rownaghi, A. A.; Rezaei, F. Development and Assessment of Magnetic Fe₂O₃@MOF-74 Composite Sorbents for Ethylene/Ethane Separation. *Chem. Eng. J.* **2023**, *451*, 139006.
- (41) Ambroz, F.; Macdonald, T. J.; Martis, V.; Parkin, I. P. Evaluation of the BET Theory for the Characterization of Meso and Microporous MOFs. *Small methods* **2018**, 2 (11), 1800173.
- (42) Thommes, M.; Kaneko, K.; Neimark, A. V.; Olivier, J. P.; Rodriguez-Reinoso, F.; Rouquerol, J.; Sing, K. S. W. Physisorption of Gases, with Special Reference to the Evaluation of Surface Area and Pore Size Distribution (IUPAC Technical Report). *Pure Appl. Chem.* **2015**, *87* (9–10), 1051–1069.
- (43) Al-Mamoori, A.; Lawson, S.; Rownaghi, A. A.; Rezaei, F. Improving Adsorptive Performance of CaO for High-Temperature CO₂ Capture through Fe and Ga Doping. *Energy Fuels* **2019**, 33 (2), 1404–1413.
- (44) Xiang, C.; Ji, Q.; Zhang, G.; Wang, H.; Qu, J. In Situ Creation of Oxygen Vacancies in Porous Bimetallic La/Zr Sorbent for Aqueous Phosphate: Hierarchical Pores Control Mass Transport and Vacancy Sites Determine Interaction. *Environ. Sci. Technol.* **2020**, *54* (1), 437–445.
- (45) Guo, H.; Feng, J.; Zhao, Y.; Wang, S.; Ma, X. Effect of Micro-Structure and Oxygen Vacancy on the Stability of (Zr-Ce)-Additive CaO-Based Sorbent in CO₂ Adsorption. *J. CO*₂ *Util.* **2017**, *19*, 165–176.
- (46) Van Miltenburg, A.; Zhu, W.; Kapteijn, F.; Moulijn, J. A. Adsorptive Separation of Light Olefin/Paraffin Mixtures. *Chem. Eng. Res. Des.* **2006**, 84 (5), 350–354.
- (47) Hartmann, M.; Böhme, U.; Hovestadt, M.; Paula, C. Adsorptive Separation of Olefin/Paraffin Mixtures with ZIF-4. *Langmuir* **2015**, *31* (45), 12382–12389.
- (48) Wu, H.; Chen, Y.; Lv, D.; Shi, R.; Chen, Y.; Li, Z.; Xia, Q. An Indium-Based Ethane-Trapping MOF for Efficient Selective Separation of C₂H₆/C₂H₄ Mixture. *Sep. Purif. Technol.* **2019**, 212, 51–56.
- (49) Al-Naddaf, Q.; Rownaghi, A. A.; Rezaei, F. Multicomponent Adsorptive Separation of CO₂, CO, CH₄, N₂, and H₂ over Core-Shell Zeolite-5A@MOF-74 Composite Adsorbents. *Chem. Eng. J.* **2020**, 384, 123251.
- (50) Lawson, S.; Al-Naddaf, Q.; Newport, K.; Rownaghi, A.; Rezaei, F. Assessment of $\rm CO_2/CH_4$ Separation Performance of 3D-Printed Carbon Monoliths in Pressure Swing Adsorption. *Ind. Eng. Chem. Res.* **2021**, *60*, 16445.
- (51) Al-Naddaf, Q.; Lawson, S.; Rownaghi, A. A.; Rezaei, F. Analysis of Dynamic Capture over Zeolite Monoliths in the Presence of and Humidity. *AIChE J.* **2020**, *66* (9), e16297.
- (52) Baamran, K.; Lawson, S.; Rownaghi, A. A.; Rezaei, F. Process Evaluation and Kinetic Analysis of 3D-Printed Monoliths Comprised of CaO and Cr/H-ZSM-5 in Combined CO $_2$ Capture-C $_2$ H $_6$ Oxidative Dehydrogenation to C $_2$ H $_4$. Chem. Eng. J. 2022, 435, 134706.
- (53) Zhou, J.; Wu, J.; Liu, Y.; Zou, F.; Wu, J.; Li, K.; Chen, Y.; Xie, J.; Ying, H. Modeling of Breakthrough Curves of Single and Quaternary Mixtures of Ethanol, Glucose, Glycerol and Acetic Acid Adsorption onto a Microporous Hyper-Cross-Linked Resin. *Bioresour. Technol.* **2013**, *143*, 360–368.